Biophysical Journal
Article

Biophysical Society

Structure and Conformation of Wild-Type Bacterial Lipopolysaccharide Layers at Air-Water Interfaces

Samantha Micciulla,[1,2] Yuri Gerelli,[1] and Emanuel Schneck[2,*]
[1]Institut Laue-Langevin, Grenoble, France and [2]Max Planck Institute of Colloids and Interfaces, Potsdam, Germany

ABSTRACT The outer membrane of Gram-negative bacteria is of great scientific interest because it mediates the action of antimicrobial agents. The membrane surface is composed of lipopolysaccharide (LPS) molecules with negatively charged oligosaccharide headgroups. To a certain fraction, LPSs additionally display linear polysaccharides termed O-side chains (OSCs). Structural studies on bacterial outer surfaces models, based on LPS monolayers at air-water interfaces, have so far dealt only with rough mutant LPSs lacking these OSCs. Here, we characterize monolayers of wild-type LPS from *Escherichia coli* O55:B5 featuring strain-specific OSCs in the presence of defined concentrations of monovalent and divalent ions. Pressure-area isotherms yield insight into in-plane molecular interactions and monolayer elastic moduli. Structural investigations by x-ray and neutron reflectometry reveal the saccharide conformation and allow quantifying the area per molecule and the fraction of LPS molecules carrying OSCs. The OSC conformation is satisfactorily described by the self-consistent field theory for end-grafted polymer brushes. The monolayers exhibit a significant structural response to divalent cations, which goes beyond generic electrostatic screening.

INTRODUCTION

Gram-negative bacteria are responsible for numerous harmful infections and are able to develop multidrug resistance (1,2). The defense mechanism of bacteria against antimicrobial molecules is thus of urgent relevance for drug development (3). A key aspect in these efforts is the unique structure of the Gram-negative bacterial outer membrane, which exhibits an asymmetric composition. While its proximal leaflet is mainly constituted by glycerophospholipids, the distal leaflet forming the actual outer surface is predominantly composed of lipopolysaccharide (LPS) molecules (4–6), which cover more than 75% percent of the surface area (7).

LPSs are amphiphilic molecules constituted of an acylated oligosaccharide (8) to which a long polysaccharide chain may be attached. In Enterobacteriaceae, like *Escherichia coli*, three fundamental building blocks can be distinguished: 1) the lipid A, which consists of a 1,4′-diphosphorylated β1.6-linked glucosamine disaccharide; 2) the core oligosaccharide, composed of 12 to 13 sugar units in wild-type bacteria; and 3) a strain-specific O-polysaccharide (O-antigen or O-side chain (OSC)), a structurally highly variable polysaccharide often built from a repetitive oligosaccharide motif. This kind of LPS is called "S-form" or "smooth" LPS. However, a significant fraction of LPS prepared from S-form LPSs lacks these OSCs, and it is referred to as "R-form" or "rough" LPS. Mutant bacteria that are unable to synthesize or attach an O-antigen are called rough mutants. Lipid A and the core are negatively charged because of the presence of two 3-deoxy-D-manno-oct-2-ulosonic acids in the inner core, phosphate, or galacturonic acid substitutions. However, net charge and distribution of the LPS charges are subject to modifications because of the removal of phosphate or addition of ethanolamine, glucosamine (GlcN), or 4-aminoarabinose. Such structural modifications, including the attachment of an O-polysaccharide, are associated with an increased resistance (e.g., against antimicrobial peptides or serum) (1). Fig. 1 schematically illustrates the structure of LPS molecules from *E. coli* serotype O55:B5. Further details on the chemical structure are given in the Materials. *E. coli* owes its relevance as part of the microbiota of the digestive system of mammals and to its emerging application as a biosensor for monitoring several cellular processes (9). Despite the harmless character of most of its strains, some serotypes are responsible for dangerous sepsis (10).

Apart from their structural role, LPS surfaces likely act as protection against harmful molecules. It has been proposed

Submitted December 4, 2018, and accepted for publication February 21, 2019.

*Correspondence: schneck@mpikg.mpg.de

Editor: Tommy Nylander.
https://doi.org/10.1016/j.bpj.2019.02.020

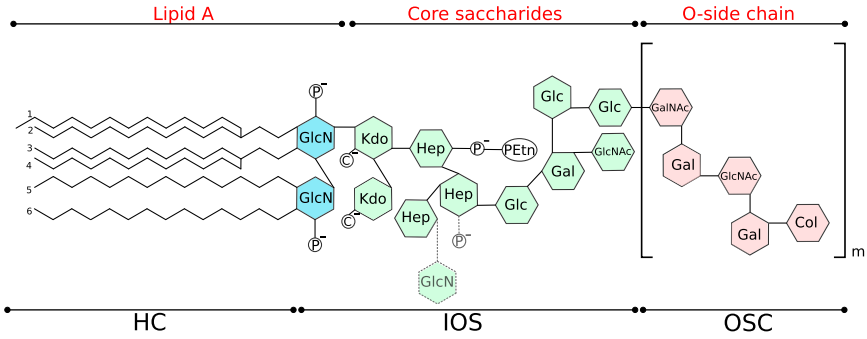

FIGURE 1 Chemical structure of wild-type lipopolysaccharides (LPSs) from *E. coli* serotype O55:B5 used in this study. The dotted line indicates the two possible structural variants of *E. coli* R3 inner core: the GlcN side-chain modification of the heptose (~30%) is only present when the phosphate at the second Hep residues is absent. P and C denote phosphate and carboxylate groups, respectively, carrying negative charges at pH = 7. Col, colitose; Gal, galactose; GalNAc, N-acetylgalactosamine; Glc, glucose; GlcNAc, N-acetylglucosamine; Hep, L- glycero-D-manno-heptoseketo-deoxyoctulosonate; Kdo, 3-deoxy-D-manno-2-octulosonic acid; PEtN, phosphorylethanolamine. To see this figure in color, go online.

that the reduced influx and uptake of antibiotics at the base of bacterial resistance is a direct consequence of the low permeability barrier provided by LPSs (3), forming a very dense structure, which limits the diffusion of both hydrophilic and hydrophobic molecules to the periplasmic space (5,11,12). Several in vivo studies showed that the sensitivity of Gram-negative bacteria to cationic antimicrobial peptides is reduced in the presence of divalent cations like Ca^{2+} or Mg^{2+}. The presence of negative charges of phosphate and carboxylate groups in the core oligosaccharide drives the condensation of divalent ions and their characteristic cross-bridging between adjacent LPS molecules (13,14). Their crucial role is further corroborated by the observation that chemical agents disrupting such cross-binding are able to permeabilize the outer membrane (15). Computer simulations involving cationic antimicrobial peptides suggested that divalent cations can suppress the penetration of the peptides into the LPS layers and therefore reduce antimicrobial activity (16). A more recent simulation study further indicated that divalent cations rigidify the outer membrane (17), which was later confirmed experimentally using interfacial shear rheometry on LPS monolayers (18).

The great biomedical relevance of Gram-negative bacterial membranes and their interactions with ions and antimicrobial molecules has motivated numerous experimental studies on LPS layers, which are well defined and meaningful model systems of the membrane outer surface. To this end, LPS monolayers at the air-water interface have been investigated intensively by x-ray and neutron scattering techniques, which are able to reveal the molecular-scale structural information required for a mechanistic understanding of the interactions at the base of many processes of biological and technological interest. Grazing-incidence x-ray diffraction showed the in-plane ordering of such monolayers in the presence and absence of divalent cations or during exposure to antimicrobial peptides (19–21). Complementary x-ray reflectometry (XRR) and neutron reflectometry (NR) measurements further revealed the density profiles perpendicular to the interface under various ion conditions (20–22). Finally, grazing-incidence x-ray fluorescence revealed excess ion amounts and distributions in LPS monolayers (14). Importantly, all these structural studies have used rough mutant LPS, which is reasoned by the ease of purification and handling compared to wild-type extracts (11) but potentially of limited biomedical relevance. To the best of our knowledge, the only study on wild-type LPS monolayers featuring the strain-specific OSCs focused on pressure-area isotherms but did not investigate structural details (23). On the other hand, the only structural characterizations of wild-type LPS layers have so far been conducted after immobilization at solid-liquid interfaces (24,25). However, for a number of reasons, the structure of wild-type LPS monolayers at air-water interfaces is of particular interest. At first, this versatile sample architecture is commonly used for structural, thermodynamic, rheological, and spectroscopic investigations of monolayers under various conditions and during exposure to antimicrobial molecules (for instance, the determination of peptide secondary structures from the amide I/II ratio (26–28)). Most of these investigations cannot be carried out with solid-supported monolayers. Secondly, LPS monolayers at air-water interfaces constitute a preparation step for the creation of more complex sample architectures on solid supports, as in the case of Langmuir-Blodgett and Langmuir-Schaefer transfer techniques (22,25,29). Finally, structural investigations by XRR and NR of LPS layers supported by hydrophobized solid substrates are often insensitive to the characteristics of the fatty acid tail layer (25), whereas there is no such limitation for monolayers at air-water interfaces.

In this work, monolayers of wild-type LPS from *E. coli* serotype O55:B5 (see Fig. 1) at air-water interfaces are investigated with pressure-area isotherms and structurally characterized by combined XRR and NR with contrast variation. Comprehensive structural insight is obtained from the complementarity of XRR and NR: while XRR offers good contrast between air and the fatty acid chains, NR is able to distinguish between water and hydrated saccharides. To investigate the influence of cations on the monolayer organization, experiments are performed at different concentrations of monovalent and divalent cations in the water

subphase. The isotherms confirm the formation of Langmuir-type monolayers, in agreement with previous findings (23), and reveal a significant influence of divalent ions on molecular packing density and in-plane compressibility. The reflectometry measurements reveal the amount and distribution of fatty acids, core saccharides, and OSCs with subnanometer spatial resolution in the direction perpendicular to the interface. In agreement with earlier studies on solid-supported LPS monolayers (25), the saccharide profiles are seen to be bimodal, with dense inner oligosaccharides (IOSs) and more dilute, extended OSCs. The ion valency is found to have a considerable influence on the monolayer structure and molecular density.

The use of wild-type LPS for structural studies has been questioned because of the hypothesis of a preferential exclusion of S-form LPS molecules from the interface into the aqueous medium over time (11). To this end, our results indicate that the fraction of S-form LPS molecules in the monolayers is conserved over timescales of several hours.

MATERIALS AND METHODS

Materials

Wild-type LPS from *E. coli* serotype O55:B5, HEPES, NaCl, $CaCl_2$, and D_2O were purchased from Sigma Aldrich (Saint-Quentin, France). The Milli-Q water (termed H_2O in the text) was obtained using a Merck Millipore purification system (Molsheim, France). All the chemicals were used as received without any further purification.

The chemical structure of the wild-type LPS molecules is schematically illustrated in Fig. 1. The lipid A has six hydrocarbon chains (HCs), four C14-β-hydroxy acyl chains attached to the GlcN sugars and two acyl chains, C14 and C12, attached to the β-hydroxy group (12). It includes two GlcNs with phosphate groups. The core saccharide (type R3) (30–32) is constituted by 12 monosaccharides and carries four negative charges at pH = 7. The inner part has two 3-deoxy-D-manno-2-octulosonic acid, three L-glycero-D-manno-heptose, and one phosphorylethanolamine. Noteworthy, a minor fraction ($\approx$30%) of *E. coli* R3 core is a structural variant containing a GlcN substitution of the side-chain heptose (Fig. 1, *dotted line*) (33). The biosynthetic pathway for the GlcN modification requires the removal of the phosphate on the second heptose by a phosphatase (32). The outer part is formed by one N-acetylglucosamine, three glucose, and one galactose unit. The last domain, the OSC, is a polydisperse polymer of an uncharged linear pentasaccharide (34). The repeating unit is composed of one N-acetylglucosamine unit, two galactose units, one N-acetylgalactosamine, and one colitose unit.

For the analysis of the reflectivity profiles, the LPS structure was conveniently divided into three regions (see Fig. 1): 1) the HCs; 2) the IOS formed by the two phosphorylated GlcN moieties of lipid A and the core saccharide of rough mutant LPS; and 3) the strain-specific OSC.

Sample preparation

Aqueous subphases for Langmuir isotherms and XRR experiments were prepared from 10 mM HEPES in Milli-Q water (18 MΩ cm) solution at pH 7.4. For NR experiments, the buffer was prepared either in D_2O or in an H_2O-D_2O mixture termed air contrast matched water (ACMW; 92:8 H_2O-D_2O v/v). From the buffer solution, termed low-salt subphase, two additional subphases were prepared: a Ca^{2+}-free subphase by addition of 100 mM NaCl and a Ca^{2+}-loaded subphase by addition of 100 mM NaCl and 20 mM $CaCl_2$. LPS solutions were prepared according to a procedure reported by Katsaras and co-workers (23): liquid phenol, chloroform, and petroleum ether were mixed at the volume ratio (2:5:8), in which LPS was dissolved for a final concentration of 1 mg/mL. The solution was stored at -20°C and sonicated for 10 min at room temperature before use.

Pressure-area isotherms

Pressure-area isotherms were measured on a Nima 1212D Langmuir trough (Nima Technology, Coventry, UK) available at the Partnership for Soft Condensed Matter (Grenoble, France). In the first step, 450 μL of LPS solution was spread onto an aqueous subphase at an initial area of 1120 cm^2. To promote the formation of a monolayer at the air-water interface, after the complete evaporation of the organic solvent, the area was reduced by moving a polytetrafluoroethylene barrier at a constant speed of 30 cm^2/min until reaching a surface pressure of $\Pi = 45$ mN/m. Subsequent compression-expansion cycles were run at the same barrier speed. The monolayer stability was investigated by measuring the change of surface pressure π as a function of time for two selected, fixed pressures of 15 and 30 mN/m while the barrier position was kept constant. The surface pressure was determined by a filter-paper Wilhelmy plate monitoring the force applied on the partially submerged plate. This force is then converted into surface tension γ (mN/m). The corresponding surface pressure is $\Pi = \gamma_0 - \gamma$, where γ_0 is the surface tension of the bare air-water interface, and γ is the surface tension in the presence of the monolayer at a given accessible area.

XRR and NR

XRR experiments were performed with an Empyrean diffractometer from Malvern Panalytical (Limeil-Brevannes, France) with a PIXcel^{3D} scintillator detector. The experiments were performed in $\theta/2\theta$ geometry, where the incident angle θ was varied from 0.025° to 3° in steps of 0.005° or 0.01°. The monochromatic x-ray source was a Cu anode emitting K_α radiation (wavelength $\lambda = 1.54$ Å). On the incoming beam side, a divergence slit of 1/32°, parafocusing optics, and antiscatter slit of 1/16° were used. Between mirror and antiscatter slit, a Soller slit of 0.04° was used to reduce the horizontal beam divergence. On the detector site, an antiscatter slit and a receiving slit of 1/32° were used.

NR experiments (35) were performed at the time-of-flight reflectometer FIGARO (36) at the Institut Laue-Langevin (Grenoble, France) with a wavelength range of 2.5 Å $< \lambda <$ 16 Å. Two fixed angles of incidence, $\theta = 0.62°$ and 3.78°, were selected. The experimental resolution in q_z, ($\Delta q_z/q_z$), defined as the full width at half maximum, was $\approx$9%.

Irrespective of the type of radiation used (x-rays or neutrons), the reflectivity, R, that is, the reflected intensity relative to the intensity of the incident beam, is recorded as a function of the component of the scattering vector perpendicular to the interface, $q_z = (4\pi/\lambda)\sin\theta$. The reflectivity curve $R(q_z)$ depends on the depth profile of the scattering length density (SLD), $\rho(z)$, across the interface between two bulk media (air and water in the experiments described here). For each chemical component, the s-ray SLD is proportional to the electron density, whereas the neutron SLD is a function of the number density of the constituting nuclides and of their coherent scattering length b_i,

$$\rho_i = \sum \left(\frac{n_i}{\nu}\right) b_i, \qquad (1)$$

where n_i is the number of nuclides i per molecule and ν the molecular volume. With that, the distributions of all components, with characteristic SLDs, can be reconstructed from $R(q_z)$. To avoid ambiguities in this procedure and to enhance the accuracy in the determination of the location of the chemical components of interest, XRR and NR are combined, and contrast variation in NR is employed: by exploiting the large difference in the scattering lengths of the hydrogen isotopes H and D, the SLD of the aqueous medium is varied in this study using either D_2O ($\rho_{D_2O} = 6.36 \times 10^{-6}$ Å^{-2}) or ACMW ($\rho_{ACMW} = \rho_{air} = 0$).

For the reflectivity experiments, a solution of LPS was spread onto a Ca^{2+}-free or Ca^{2+}-loaded subphase (see Sample Preparation). The amount of material needed to reach a surface pressure of $\Pi = 15$ mN/m, as motivated in the Results and Discussion, was deposited onto the aqueous surface. For NR experiments, buffer solutions based on D_2O and on ACMW were used.

Reflectivity data analysis

The model used for reflectivity analysis is based on the volume fraction profiles, $\phi_i(z)$, of all chemical components perpendicular to the interface (37) and for each sample simultaneously describes the NR curves in both D_2O buffer and ACMW buffer contrasts and the x-ray reflectivity curve in H_2O buffer. The components considered in the model are HCs (i = HC), IOSs (i = IOS), OSCs (i = OSC), and water (i = W). The SLD profile for each condition is then as follows:

$$\rho^{(x,n)}(z) = \phi_{HC}(z)\rho_{HC}^{(x,n)} + \phi_{IOS}(z)\rho_{IOS}^{(x,n)} + \phi_{OSC}(z)\rho_{OSC}^{(x,n)} + \phi_{W}(z)\rho_{W}^{(x,n)}. \quad (2)$$

The distance measured perpendicular to the surface is denoted with z, where $z = 0$ is arbitrarily taken at the interface between air and the HCs. The x-ray and neutron SLDs of the i-th component are denoted with ρ_i^x and ρ_i^n, respectively. For the HCs, $\rho_{HC}^x = 8.0 \times 10^{-6}$ Å^{-2} and $\rho_{HC}^n = -0.4 \times 10^{-6}$ Å^{-2} are assumed (29,38,39). The SLDs of IOS and OSC were estimated from the molecular volumes and from the atomic-isotopic composition (25). For x-rays, the values of $\rho_{IOS}^x = 15.2 \times 10^{-6}$ Å^{-2} and $\rho_{OSC}^x = 14.2 \times 10^{-6}$ Å^{-2} are obtained. Because of the dynamic exchange of labile hydrogens with the solvent, the neutron SLDs of IOS and OSC depend on the H_2O-D_2O ratio of their aqueous environment (with SLD ρ_W^n), which leads to the relation $\rho_{IOS}^n = 2.08 \times 10^{-6}$ Å^{-2} + $0.41\rho_W^n$ and $\rho_{OSC}^n = 1.77 \times 10^{-6}$ Å^{-2} + $0.34\rho_W^n$.

In the theoretical volume fraction profile (Fig. 2), the distributions of HC and IOS, $\phi_{HC}(z)$ and $\phi_{IOS}(z)$, respectively, are represented as adjacent homogeneous slabs modulated by error functions with adjustable roughness parameters $\xi_{A/HC}$, $\xi_{HC/IOS}$, and $\xi_{IOS/OSC}$, where the latter accounts for the roughness of the interface between the IOS layer and the aqueous medium accommodating the OSC. The layer thicknesses d_{HC} and d_{IOS} are adjustable parameters. The water fraction in the IOS layer, ϕ_W^{IOS}, is also an adjustable parameter, whereas the hydrophobic HC layer is assumed to be water free. Instead, the model accounts for a fraction of free "cavities" or "voids" (ϕ_{FV}^{HC}) in the HC layer. Based on the results of a previous study (25), the OSC profile is modeled with a stretched exponential function,

$$\phi_{OSC}(z) = I(z)\phi_0 \exp^{-|z/\Lambda|^n}, \quad (3)$$

where ϕ_0 is the maximal OSC volume fraction at the interface with the IOS layer, and Λ represents the OSC extension. The value of the stretching exponent n further affects the shape of the profile, so that Eq. 3 allows describing a wide range of shapes with only few model parameters. The factor $I(z)$ is characterized by the parameter $\xi_{IOS/OSC}$ (as mentioned above) and describes the roughness of the IOS layer outer surface, to which the OSCs are "grafted."

The amount of each chemical component is expressed in volume per surface area and calculated by integrating the volume fraction distribution of the i-th component over the z axis,

$$D_i = \int_{-\infty}^{+\infty} \phi_i(z)dz. \quad (4)$$

Here, D_i has the unit of a linear dimension and corresponds to the thickness of an equivalent layer composed entirely of component i, where $\phi_i(z) = 1$. The use of this quantity enables comparison between the amounts of different chemical components irrespective of the details of their interfacial distribution.

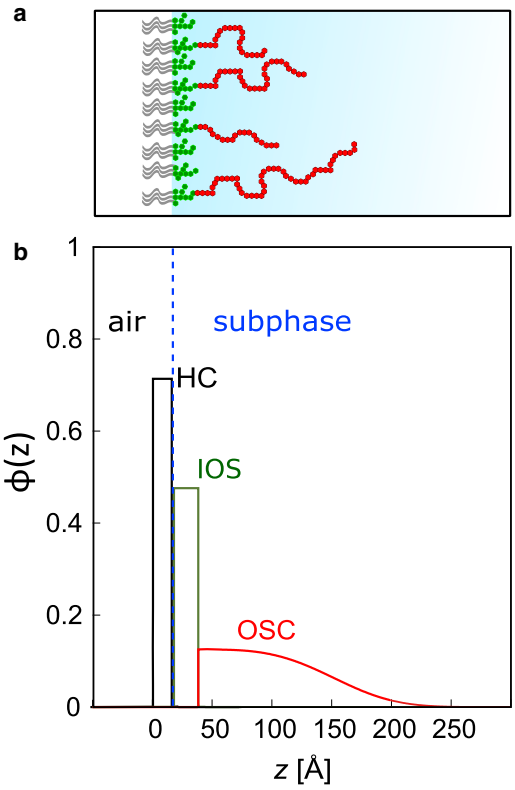

FIGURE 2 (*a*) Schematic representation of a wild-type LPS monolayer at an air-water interface. (*b*) An illustration of the theoretical model used to interpret the experimental reflectivity data is shown. The model is based on the volume fraction profiles of the chemical components perpendicular to the interface. The components are hydrocarbon chains (HCs), inner oligosaccharides (IOSs) and O-side chains (OSCs); the air and the liquid subphase constitute the bulk media. The dotted line traces the position of the HC-IOS interface, that is, the hydrophobic-hydrophilic interface. To see this figure in color, go online.

For a given IOS amount per unit area, D_{IOS}, the water fraction inside the layer, ϕ_W^{IOS}, is not an independent parameter but follows from d_{IOS} and the normalization condition expressed in Eq. 4. Namely, $D_{IOS} = \int_{-\infty}^{+\infty} \phi_{IOS}(z)dz = (1 - \phi_W^{IOS})\, d_{IOS}$, so that $\phi_W^{IOS} = 1 - D_{IOS}/d_{IOS}$. Similarly, ϕ_{FV}^{HC} is dictated by D_{HC} and D_{HC}, whereas ϕ_0^{OSC} is dictated by D_{OSC}, Λ, and n. Finally, D_{IOS} and D_{HC} are coupled by an adjustable proportionality factor, which is common to all subphases and reflects the fixed stoichiometry of HC and IOS moieties.

As in earlier studies (37,40), ideal mixing of all components is assumed, such that the sum of all volume fractions in the model is equal to 1 at each z-position:

$$\sum \phi_i(z) \equiv 1. \quad (5)$$

Water is required to occupy the space free of the other components, and $\phi_W(z)$ directly follows from Eq. 5.

A fit of the theoretical model to the experimental reflectivity curves, obtained by the optimization of the adjustable parameters, is performed as follows: sets of initial parameters are chosen to calculate the corresponding x-ray SLD profile $\rho^x(z)$ and the neutron SLD profiles $\rho^n(z)$ for D_2O and ACMW contrasts. The profiles are then discretized into hundreds of thin slabs of 1 Å thickness with constant SLD, and the corresponding

q_z-dependent reflectivity curves are calculated from the Fresnel reflection laws at each slab-slab interface using the iterative recipe of Parratt (41). To account for the finite experimental q_z resolution, all the theoretical reflectivity curves calculated for infinite resolution are convoluted with Gaussian functions representing the experimental resolution. All parameters are varied until the best simultaneous agreement with all experimental data is reached by χ^2 minimization. To give x-ray and neutron reflectivity curves comparable weights in the fit, the χ^2 value associated with the neutron data, which have fewer data points and larger statistical errors, was multiplied by an amplification factor. Although the choice of this factor is not unique, it was aimed at achieving equally good simultaneous agreement of the model with x-ray and neutron data and thus at obtaining the most robust possible results. Purely statistical error estimates, which are strictly valid only within the framework of a "perfect model," typically underestimate the real parameter uncertainties due to systematic errors. For this reason, we provide more conservative error estimates that approximately also reflect the variation of the obtained parameters with respect to variations in the model parametrization. As pointed out earlier (40), we consider these larger error estimates more meaningful.

RESULTS AND DISCUSSION

The LPS monolayers are investigated on three different aqueous subphases: the low-salt subphase containing 10 mM HEPES buffer (see Sample Preparation), the Ca^{2+}-free subphase with additional 100 mM of monovalent salt NaCl to obtain approximately physiological ionic strength, and the Ca^{2+}-loaded subphase containing 20 mM $CaCl_2$ on top of the monovalent salt to investigate the influence of divalent cations. This calcium concentration lies well above the physiological concentration of around 1–2 mM (42) but allows for a better comparability with earlier studies that commonly involved elevated calcium concentrations (20,21,25).

LPS in-plane interactions and monolayer stability

A pressure-area isotherm is a representation of the monolayer pressure π as a function of the molecular area A. Fig. 3 shows isotherms upon the first compression of LPS monolayers on low-salt, Ca^{2+}-free, and Ca^{2+}-loaded subphases. Because the ratio of R-form and S-form LPS molecules in the monolayer, and thus also the average molecular mass, are unknown, the surface area is normalized by the LPS spread mass rather than by the number of molecules. The top abscissa reporting the area per molecule A_{LPS} is based on the reflectivity analysis (see text further below).

As seen in the plot, the pressure increases monotonically with decreasing surface area up to $\Pi = 45$ mN/m without any evidence of monolayer collapse. An indicator of the range of the in-plane molecular interactions is the onset of the pressure increase, which we define as the specific area at which Π reaches 2.0 mN/m, noting that this definition is not unique. This specific area at onset decreases from ≈ 1.35 cm$^2/\mu$g on low-salt subphase to ≈ 1.25 cm$^2/\mu$g on Ca^{2+}-free subphase to ≈ 0.80 cm$^2/\mu$g on Ca^{2+}-loaded subphase, meaning that repulsive molecular interactions become more short range by the addition of 100 mM monovalent salt

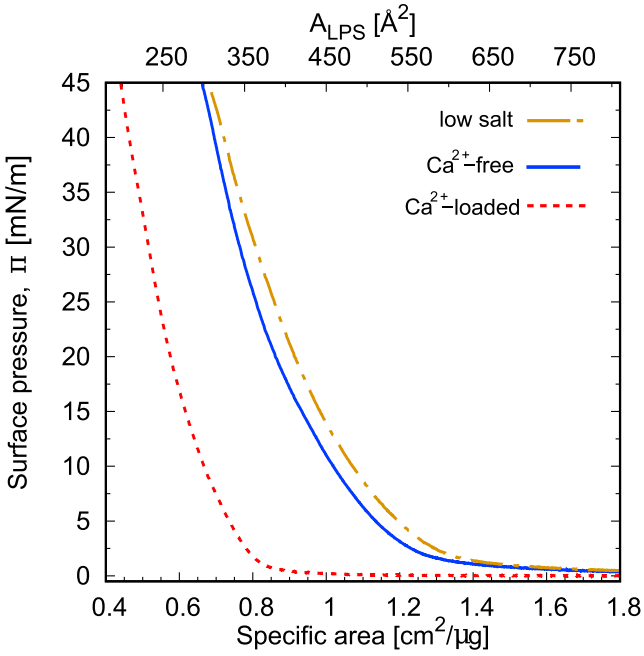

FIGURE 3 Langmuir isotherms of wild-type LPS on low-salt, Ca^{2+}-free, and Ca^{2+}-loaded subphases. The bottom abscissa represents the surface area normalized by the amount of the spread LPS, whereas the top abscissa is the area per molecule as estimated by reflectometry (see Results and Discussion). To see this figure in color, go online.

and even more by further adding 20 mM divalent cations. Given the LPS chemical composition (Fig. 1), one can consider the molecular interactions as a combination of electrostatic repulsion between the charged sugar units in IOS, steric repulsion between adjacent charge-neutral OSCs, and finally the interaction between alkyl chains. The pronounced influence of the added ions on the specific area at onset and on the isotherms in general demonstrates that the electrostatic repulsion between the charged moieties is more important than the salt-independent steric repulsion between the charge-neutral OSC. The fact that the curves do not converge even at high pressures further indicates that the interaction is never fully dominated by the steric interaction between the alkyl chains but reflects electrostatic repulsion at least on low-salt and Ca^{2+}-free subphases. This result is consistent with the density reduction reported earlier when solid-supported LPS monolayers were subject to calcium depletion (25). The specific surface areas reached at $\Pi = 45$ mN/m are 0.68, 0.66, and 0.44 cm$^2/\mu$g on low-salt, Ca^{2+}-free, and Ca^{2+}-loaded subphases, respectively. Again, the presence of 100 mM monovalent ions in the subphase has only a minor influence; in contrast, when 20 mM divalent cations are added, a significantly smaller specific area can be achieved at a given pressure, in good agreement with previous reports on monolayers of R-form and S-form LPS (18,21,23). These results are a qualitative indication that the influence of ions on the monolayer structure is more dependent on the nature of the ion species than on the ionic strength alone.

To further quantify the effect of ions on the electrostatic repulsion, we calculate the generic electrostatic screening in terms of the Debye length κ^{-1} of the three subphases, resulting in $\kappa^{-1} = 22$ Å, $\kappa^{-1} = 9$ Å, and $\kappa^{-1} = 8$ Å for low-salt, Ca^{2+}-free, and Ca^{2+}-loaded subphases, respectively. Interestingly, for the higher increment of electrostatic screening ($\Delta\kappa^{-1} \approx 13$ Å upon addition of 100 mM monovalent salt), only a small change in the isotherm is observed, whereas with a minor screening increment ($\Delta\kappa^{-1} \approx 1$ Å upon further addition of 20 mM calcium ions), the range of the intermolecular repulsion is drastically reduced. This apparent mismatch clearly suggests that the influence of Ca^{2+} goes beyond generic electrostatic screening, and it has to be attributed to ion-specific bridging with negatively charged phosphate and carboxylate groups (43). This is in agreement with the results of Jeworrek et al. (21) for R-form LPS, where the binding of calcium to phosphate and carboxylate induces a smaller lateral domain size and drives the upright orientation of the sugar moieties.

Divalent cations have also been reported to affect the rigidity of LPS monolayers in terms of the surface compressive modulus (21) and the shear elastic modulus (18), albeit the latter for R-form LPS only. In the following, we calculate the surface compressive modulus, E_S (23,44), for wild-type LPS monolayers on Ca^{2+}-free and Ca^{2+}-loaded subphases:

$$E_s = -A\frac{d\pi}{dA}. \quad (6)$$

Given this definition of E_S, the modulus is higher for more rigid monolayers. The obtained values for low ($\Pi \approx 1$ mN/m), intermediate ($\Pi \approx 15$ mN/m), and high ($\Pi \approx 30$ mN/m) surface pressures are reported in Table 1. Besides the enhanced monolayer rigidity expected under increasing confinement, there is a clear increase in E_S when divalent cations interact with the sugar units. Interestingly, the values of E_S at high compression are about two times higher than those reported for deep rough mutant LPS Re from *Salmonella minnesota* (21) but about two times lower than those obtained for wild-type LPS from *Pseudomonas aeruginosa* (23). Because all these monolayers comprise a similar core saccharide structure (45,46) but differ with respect to the OSC, this observation suggests that the OSCs have a significant influence on the monolayer rigidity.

Despite their biological relevance as bacterial outer surface models, LPS monolayers comprising S-form LPS molecules have been used only in very few studies (24,25,47) because of the comparatively more difficult handling than that of rough mutant LPS. In fact, the stability of LPS monolayers including OSC-bearing S-form species at air-water interfaces has previously been questioned (11) and is addressed in this work, given that the interfacial mass conservation over long timescales is a fundamental requirement for many types of experiments. As shown in Fig. 4 *a* for LPS on Ca^{2+}-loaded subphase, subsequent cycles present two common features: 1) a hysteresis between each compression and retraction cycle (*blue* versus *red traces*), and 2) a minor mass loss ($\approx$3 and 1% for Ca^{2+}-free and Ca^{2+}-loaded LPSs, respectively) between each subsequent cycle. The kinetics of the area reduction exhibits a dependence on the applied lateral pressure (Fig. 4, *b* and *c*): at an initial pressure of $\Pi = 15$ mN/m and constant surface area, the pressure decreases with $d\Pi/dt \approx 0.05$ mN/m^{-1} min^{-1}, whereas for initial $\Pi = 30$ mN/m, the pressure decreases about two times as fast ($d\Pi/dt \approx 0.1$ mN/m^{-1} min^{-1}). A key question at this point is whether the observed pressure decrease indicates a preferential exclusion of S-form LPS from the interface toward the aqueous phase. Langmuir isotherms alone cannot clarify this aspect, which can be instead resolved from the reflectivity data discussed in the next section.

TABLE 1 Surface Compressive Moduli E_s for Wild-Type LPS Monolayers on Ca^{2+}-Free and Ca^{2+}-Loaded Subphases at $\Pi \approx 1$ mN/m, $\Pi \approx 15$ mN/m, and $\Pi \approx 30$ mN/m, Denoted as Low, Intermediate, and High Surface Pressure, Respectively

	E_S (mN/m)		
LPS Subphase	Low π	Intermediate π	High π
Ca^{2+}-free	2	58	80
Ca^{2+}-loaded	14	61	99

Monolayer structure and LPS conformation

XRR and NR experiments were performed to characterize the internal structure of the LPS monolayers on Ca^{2+}-free and Ca^{2+}-loaded subphases. Because of the slower pressure decrease over time at lower initial pressures (see previous section), the reflectivity curves were recorded at $\Pi \approx 15$ mN/m, noting that this value is somewhat lower than the consensus lateral pressure in cell membranes (20–30 mN/m) (11,44). The combined use of XRR and NR as complementary probes is crucial for a comprehensive structural characterization: while XRR offers good contrast between air and the fatty acid chains, NR is better suited to distinguish between water and hydrated saccharides. The reflectivity curves are shown in Fig. 5 for all contrast conditions, that is, D_2O and ACMW (Fig. 5, *c* and *d*) and x-ray (Fig. 5, *e* and *f*). Solid lines indicate the simulated reflectivity curves according to the best-matching parameters of the common volume fraction profile model (see Materials and Methods). The relevant features in the D_2O contrast are highlighted in the plot by dividing the experimental and simulated reflectivity curves by the Fresnel reflectivity R_F of an ideal air-D_2O interface (48). The reflectivity oscillations around 0.02 Å$^{-1} < q_z < 0.06$ Å^{-1} in both neutron contrasts are mainly due to the SLD variations associated with the hydrated extended saccharide layers. The reflectivity minima at around 0.15 Å$^{-1} < q_z < 0.20$ Å^{-1} in the x-ray contrast are caused by the less hydrated LPS moieties, especially by

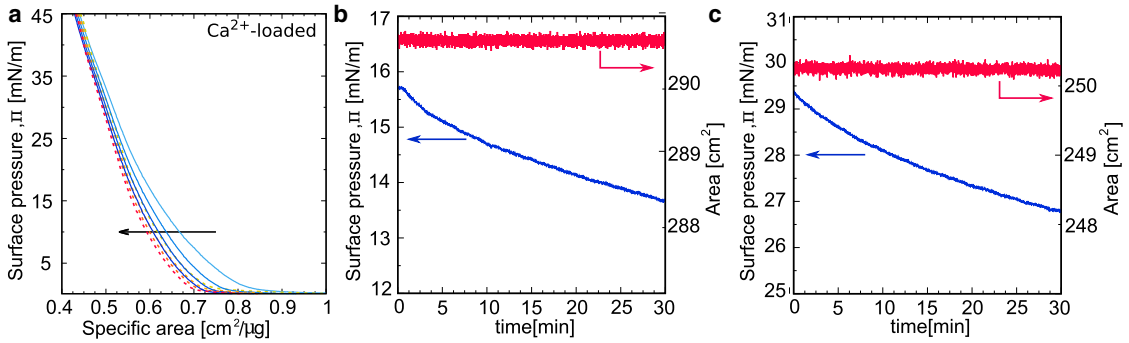

FIGURE 4 (*a*) Repeating compression (*blue solid lines*) and retraction (*red dotted lines*) cycles of wild-type LPS monolayers on a Ca^{2+}-loaded subphase. The arrow indicates the direction of subsequent compression-retraction cycles, from first to fourth. Similarly, the color intensity from light to dark corresponds to the increasing cycle number from first to fourth. (*b* and *c*) The evolution of surface pressure over time at a constant area starting with an initial surface pressure of ≈15 mN/m (*b*) and ≈30 mN/m (*c*) is shown. To see this figure in color, go online.

the dense HC layer. The shift upon calcium addition in the position of the minimum in the x-ray intensity from $q_z \approx 0.16$ Å^{-1} to $q_z \approx 0.20$ Å^{-1} reflects a calcium-induced thinning of the alkyl chains region, to which the x-rays have the highest sensitivity.

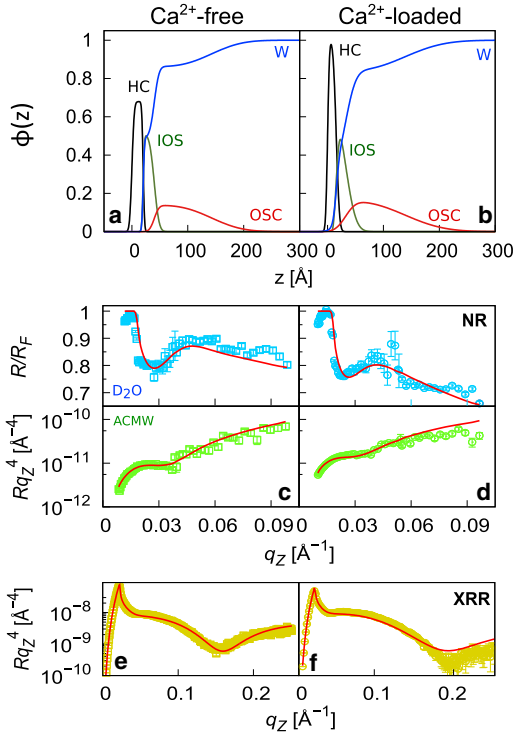

FIGURE 5 (*a* and *b*) Volume fraction profiles of chemical components in wild-type LPS monolayers on Ca^{2+}-free (*a*) and Ca^{2+}-loaded (*b*) subphases according to the best-matching parameters in the model simultaneously fitted to the neutron and x-ray reflectivity curves. (*c* and *d*) Neutron reflectivity curves in D_2O (*top*) and ACMW (*bottom*) contrast under Ca^{2+}-free (*c*) and Ca^{2+}-loaded (*d*) conditions. For clarity, the D_2O reflectivity curves are normalized by the Fresnel reflectivity R_F of an ideal air-D_2O interface (see main text). (*e* and *f*) X-ray reflectivity curves under Ca^{2+}-free (*e*) and Ca^{2+}-loaded (*f*) conditions are shown. Solid lines in (c)–(*f*) indicate the simulated reflectivity curves according the profiles shown in (*a*) and (*b*). To see this figure in color, go online.

Fig. 5, *a* and *b* show the volume fraction profiles of HC, IOS, OSC, and water corresponding to the best-matching model parameters for LPS monolayers on Ca^{2+}-free and Ca^{2+}-loaded subphases. For both subphases, the profiles evidence a defined HC layer and a bimodal saccharide distribution with a dense IOS and a more dilute, extended OSC distribution. The obtained model parameters are summarized in Table 2. The roughness of the air-HC interface is ≈3 Å for both Ca^{2+}-free and Ca^{2+}-loaded subphases, in good agreement with capillary wave theory and previous x-ray reflectivity experiments (49). The thicknesses of the HC layer, $d_{HC} \approx 20$ Å and $d_{HC} \approx 15$ Å on Ca^{2+}-free and Ca^{2+}-loaded subphases, respectively, are similar to those reported for rough mutant LPS (14–18 Å) (29). However, the comparatively high thickness value on Ca^{2+}-free subphase and the considerable cavity fraction of ≈30% (see Fig. 5 *a*) suggest that the chain layer is not compact but fairly disordered so that the projection on the surface normal results in a thicker layer (higher *d*). In contrast, when calcium ions are present, a more ordered, void-free state is established, whose effective projection results in a thinner layer (lower *d*) and compact chain configuration. This result is qualitatively different from the observation that rough mutant LPS monolayers are usually thicker under laterally more densely packed conditions (21,25) and must be attributed to the unusual structure of the LPS molecules studied here, with their bulky charged IOSs and long OSCs. With $d_{IOS} \approx 20$ Å and $d_{IOS} \approx 17$ Å on Ca^{2+}-free and Ca^{2+}-loaded subphases, respectively, the IOS layer exhibits thinning upon calcium addition and consequent roughness increment at the IOS-water interface. This result is in agreement with earlier reports (20,25), but the IOS thickness is significantly thinner than literature values (28–38 Å) (22,25). This difference must be attributed to the lower lateral density in this study ($\Pi \approx 15$ mN/m) with respect to earlier studies ($\Pi > 30$ mN/m). The lateral density can be quantified according to Eq. 4, in terms of the IOS amount per unit area, D_{IOS}, as it was established earlier for solid-supported LPS monolayers (25). D_{IOS} increases upon

TABLE 2 Best-Matching Model Parameters for Wild-Type LPS Monolayers on Ca^{2+}-Free and Ca^{2+}-Loaded Subphases at Π = 15 mN/m

Subphase	d_{HC} (Å)	d_{IOS} (Å)	$\xi_{IOS/W}$ (Å)	Λ_{OSC} (Å)	H^0_{OSC} (Å)	n	D_{IOS} (Å)	D_{OSC} (Å)	A_{LPS} (Å^2)
Ca^{2+}-free	20 (1)	20 (1)	7 (2)	119 (10)	150 (15)	1.4 (0.1)	10 (1)	15 (2)	300 (30)
Ca^{2+}-loaded	15 (1)	17 (2)	14 (2)	130 (10)	163 (15)	1.3 (0.1)	12 (1)	18 (2)	250 (30)

Parameters and associated errors (given in parentheses) are described in the main text.

addition of calcium (from ≈10 to ≈12 Å), as previously observed for solid-supported LPS monolayers, and is qualitatively consistent with the higher lateral density on Ca^{2+}-loaded subphase, as shown in the isotherms in Fig. 3. The absolute values are, however, much lower than those reported for solid-supported LPS monolayers of the same bacterial origin at a transfer pressure of 35 mN/m (D_{IOS} = 17 Å and D_{IOS} = 20 Å in the presence and absence of calcium, respectively) (25).

The area per LPS molecule can be deduced from the relation $A_{LPS} = V_{IOS}/D_{IOS}$, where $V_{IOS} \approx$ 3000 Å^3 is the IOS molecular volume (25). The resulting values are $A_{LPS} \approx$ 300 Å^2 and $A_{LPS} \approx$ 250 Å^2 on Ca^{2+}-free and Ca^{2+}-loaded subphases, respectively. Within the experimental uncertainty, the relative difference of ≈20% in A_{LPS} is roughly consistent with the relative difference of ≈30% in the specific area at Π = 15 mN/m for the two subphases in the isotherm in Fig. 3. A_{LPS} as obtained by reflectometry can thus be used for an approximate calibration of the abscissa in Fig. 3. The corresponding average molecular mass is (2.2 ± 0.3) × 10^4 g/mol. Importantly, the area per LPS molecule at the maximal compression (Π = 45 mN/m) can be reconstructed, and we obtain $A_{LPS} \approx$ 240 Å^2 and $A_{LPS} \approx$ 160 Å^2 on Ca^{2+}-free and Ca^{2+}-loaded subphases, respectively, where the latter is similar to the molecular areas reported for rough mutant LPS bilayers at high lateral compression ($A_{LPS} \approx$ 160 Å^2) (5,13). The relative difference in A_{LPS} between Ca^{2+}-free and Ca^{2+}-loaded conditions (≈50%) must be attributed to electrostatic repulsion.

The ratios of the OSC and IOS amounts per unit area, D_{OSC}/D_{IOS}, obtained on Ca^{2+}-free and Ca^{2+}-loaded subphases, are ≈1.5 and ≈1.6, respectively, and self-consistent within the experimental uncertainty. These values obtained with monolayers of an ∼1 h age agree with those reported for solid-supported LPS monolayers of the same origin, which were transferred to the solid surface right after monolayer preparation and for which $D_{OSC}/D_{IOS} \approx$ 1.3–1.5 (25). This result suggests that the fraction of S-form LPSs is a conserved quantity on the timescale of several hours. With that, the decrease in the lateral pressure over time discussed above (see Fig. 4) does not seem to reflect the preferential exclusion of S-form LPS molecules (11), but other processes, such as solubilization of non-LPS impurities, the solubilization of aggregates comprising R-form and S-form LPSs at representative stoichiometry, or rearrangements without material loss. In view of the great variability of the OSC chemistry, including neutral and charged oligosaccharides (24), we, however, refrain from generalizing this conclusion to all types of wild-type LPSs.

The OSC conformations are characterized by the volume fraction profiles in Fig. 5, *a* and *b* and the associated parameters Λ and n (Eq. 3), reported in Table 2. The obtained OSC extensions in terms of the decay lengths are $\Lambda \approx$ 120 Å and $\Lambda \approx$ 130 Å on Ca^{2+}-free and Ca^{2+}-loaded subphases, respectively. The equivalent maximal brush extensions $H_0 = \Lambda\sqrt{1-e^{-1}}$ (50) correspond to $H_0 \approx$ 150 Å and $H_0 \approx$ 163 Å. It is seen that the OSC conformation is similar on the two subphases, which is not surprising because of the absence of charges on OSC units. The slightly larger extension on the Ca^{2+}-loaded subphase can be considered an effect of the higher lateral density and can be rationalized within the framework of the self-consistent field (SCF) theory (51), which strictly holds for dense, monodisperse polymer brushes:

$$H_0(\sigma, N) = aN\left(\frac{8p\tau}{\pi^2}\right)^{1/3}\left(a^2\sigma\right)^{1/3}, \tag{7}$$

where σ is the grafting density, $a \approx$ 5.9 Å the linear dimension of a sugar monomer (25), N = 5 m the number of sugar monomers per chain (see Fig. 1), and $p\tau \approx$ 1 (25). Importantly, $H_0 \propto \sigma^{1/3} \propto A_{LPS}^{-1/3}$. Accordingly, a 6% increase in H_0 (∼10 Å) is expected upon lateral compression from A_{LPS} = 300 Å^2 to A_{LPS} = 250 Å^2, in good agreement with the obtained values. The same reasoning also holds for the comparison with the larger OSC extension ($H_0 \approx$ 180 Å) obtained at the solid-liquid interface in presence of calcium for higher lateral densities ($A_{LPS} \approx$ 160 Å^2) (25), where Eq. 7 predicts a difference in H_0 of ∼25 Å, in rough agreement with the obtained difference of 17 Å. In summary, the conformation of uncharged OSCs appears to be reasonably well described by the SCF theory for polymer brushes.

Coming back to the scenario of preferential exclusion of S-form LPS molecules from the monolayer over time, we notice that the free energy associated with this process is a balance between the OSC conformational free energy per molecule, F_{conf}, favoring exclusion, and the alkyl chain solvation free energy per molecule, F_{solv}, opposing it. The former can be estimated as follows (52):

$$\frac{F_{conf}}{k_BT} \approx \frac{h^2}{2a^2N} + \frac{\nu N^2\tilde{\sigma}}{2ha^2}, \tag{8}$$

where h is the stretched polymer height (with $h \approx H_0$), $\tilde{\sigma} = \sigma a^2$ the reduced grafting density, $N \approx$ 90 the number

of monomer units (25), and $\nu = a^3(1 - 2\chi)$, with $\chi \approx 0.4$ for a good solvent. For the given OSC grafting densities, we obtain $F_{\mathrm{conf}} \approx 10$ kJ/mol (or 4 k_BT), irrespective of the subphase. F_{solv} can be roughly estimated by considering the solvation free energy per CH_2 in water, $\Delta G^0_{CH_2} \approx 2.8$ kJ/mol (53). Assuming that only half of the CH_2 units of a molecule are exposed to water, we obtain $F_{\mathrm{solv}} \approx 100$ kJ/mol (or 40 k_BT), meaning that the LPS solvation has a high energetic cost. An alternative, consistent estimate approximates the chain region as a spherical oil droplet of volume $V = d_{HC}A_{LPS} \approx 3900$ Å^3 and radius ≈ 9 Å, whose interface with the aqueous medium has a tension somewhat below the 56 mN/m reported for macroscopic interfaces (54,55) because of the subnanometer radius (56). Although these estimates neglect the effect of aggregate formation, which can considerably reduce the solvation free energy per molecule, the magnitude of F_{solv} will likely remain much higher than that of F_{conf} so that a predominance of the conformational free energy, and thus preferential solubilization of S-form LPS molecules, appears to be unlikely, in agreement with our experimental observations.

CONCLUSIONS

We have comprehensively characterized wild-type LPS monolayers at the interface between air and aqueous solutions containing various defined concentrations of monovalent and divalent cations. Pressure-area isotherms yield insight into the contributions of electrostatic and OSC-induced (polymer-steric) forces on the in-plane molecular interactions and monolayer elastic moduli. The influence of divalent cations is found to go beyond generic electrostatic screening and thus to involve ion-specific bridging with negatively charged phosphate and carboxylate groups, in agreement with earlier studies on rough mutant LPS.

The structural characterization of the LPS monolayers by combined XRR and NR confirms the bimodal saccharide distribution expected from the LPS chemical structure: a dense and compact layer accommodating the negatively charged IOS and a more dilute, extended region accommodating the OSC bound to the S-form LPS molecules. The monolayers exhibit a significant structural response to the presence of divalent cations, which mostly affect the dense HC and IOS layers but indirectly also the OSC distribution via a change in the area per LPS molecule. Importantly, reflectometry allows directly quantifying the area per molecule and the fraction of S-form LPS molecules. These quantities are found to be consistent with an earlier study on LPS monolayers from the same strain at a solid-liquid interface and indicate that on experimental timescales, there is no significant preferential exclusion of S-form LPS molecules from monolayers at air-water interfaces, at least for the investigated LPS type. Comparison between reflectivity measurements at different areas per molecule reveals that the conformation of the uncharged OSC is satisfactorily described by the SCF theory for end-grafted polymer brushes.

SUPPORTING MATERIAL

Supporting Material can be found with this article online at https://doi.org/10.1016/j.bpj.2019.02.020.

AUTHOR CONTRIBUTIONS

S.M. and E.S. designed the project. S.M. carried out the experiments. Y.G. supported the NR experiments. E.S. and S.M. analyzed the data and wrote the article.

ACKNOWLEDGMENTS

The authors thank for financial support by the Max Planck Society and by the German Federal Ministry of Research and Education within the Röntgen-Ångström cluster (grant *3PhaseNR* 05K16ECA). The Institut Laue-Langevin is acknowledged for providing beam time (LTP-9-7(35)), the Partnership for Soft Condensed Matter at the Institut Laue-Langevin for the use of sample preparation laboratories, equipment and instruments, and Giovanna Fragneto for the scientific support within the Soft Matter Science and Support group at the Institut Laue-Langevin. We acknowledge Ignacio Rodriguez-Loureiro for support for data analysis and Thomas Gutsmann and Sven Müller-Loennies for insightful comments. E.S. acknowledges support from an Emmy-Noether grant (SCHN 1396/1) of the German Research Foundation.

REFERENCES

1. Delcour, A. H. 2009. Outer membrane permeability and antibiotic resistance. *Biochim. Biophys. Acta.* 1794:808–816.
2. Livermore, D. M. 2012. Fourteen years in resistance. *Int. J. Antimicrob. Agents.* 39:283–294.
3. Zgurskaya, H. I., C. A. Löpez, and S. Gnanakaran. 2015. Permeability barrier of gram-negative cell envelopes and approaches to bypass it. *ACS Infect. Dis.* 1:512–522.
4. Silhavy, T. J., D. Kahne, and S. Walker. 2010. The bacterial cell envelope. *Cold Spring Harb. Perspect. Biol.* 2:a000414.
5. Snyder, D. S., and T. J. McIntosh. 2000. The lipopolysaccharide barrier: correlation of antibiotic susceptibility with antibiotic permeability and fluorescent probe binding kinetics. *Biochemistry.* 39:11777–11787.
6. Lüderitz, O., M. A. Freudenberg, …, D. H. Shaw. 1982. Lipopolysaccharides of gram-negative bacteria. *In* Membrane Lipids of Prokaryotes. Current Topics in Membranes and Transport F. Bronner and A. Kleinteller, eds. . Academic Press, pp. 79–151.
7. Papo, N., and Y. Shai. 2005. A molecular mechanism for lipopolysaccharide protection of Gram-negative bacteria from antimicrobial peptides. *J. Biol. Chem.* 280:10378–10387.
8. Amor, K., D. E. Heinrichs, …, C. Whitfield. 2000. Distribution of core oligosaccharide types in lipopolysaccharides from Escherichia coli. *Infect. Immun.* 68:1116–1124.
9. Naurú Idalia, V.-M., and F. Bernardo. 2017. Escherichia coli as a model organism and its application in biotechnology. *In* Escherichia coli: Recent Advances on Physiology, Pathogenesis and Biotechnological Application. A. Samie, ed. IntechOpen, pp. 1309–2147.
10. Kaper, J. B., J. P. Nataro, and H. L. T. Mobley. 2004. Pathogenic Escherichia coli. *Nat. Rev. Microbiol.* 2:123–140.

11. Le Brun, A. P., L. A. Clifton, …, S. A. Holt. 2013. Structural characterization of a model gram-negative bacterial surface using lipopolysaccharides from rough strains of Escherichia coli. *Biomacromolecules.* 14:2014–2022.

12. Raetz, C. R. H., Z. Guan, …, J. Zhao. 2009. Discovery of new biosynthetic pathways: the lipid A story. *J. Lipid Res.* 50 (*Suppl*):S103–S108.

13. Snyder, S., D. Kim, and T. J. McIntosh. 1999. Lipopolysaccharide bilayer structure: effect of chemotype, core mutations, divalent cations, and temperature. *Biochemistry.* 38:10758–10767.

14. Schneck, E., T. Schubert, …, M. Tanaka. 2010. Quantitative determination of ion distributions in bacterial lipopolysaccharide membranes by grazing-incidence X-ray fluorescence. *Proc. Natl. Acad. Sci. USA.* 107:9147–9151.

15. Vaara, M. 1992. Agents that increase the permeability of the outer membrane. *Microbiol. Rev.* 56:395–411.

16. Lins, R. D., and T. P. Straatsma. 2001. Computer simulation of the rough lipopolysaccharide membrane of Pseudomonas aeruginosa. *Biophys. J.* 81:1037–1046.

17. Lam, N. H., Z. Ma, and B. Y. Ha. 2014. Electrostatic modification of the lipopolysaccharide layer: competing effects of divalent cations and polycationic or polyanionic molecules. *Soft Matter.* 10:7528–7544.

18. Herrmann, M., E. Schneck, …, M. Tanaka. 2015. Bacterial lipopolysaccharides form physically cross-linked, two-dimensional gels in the presence of divalent cations. *Soft Matter.* 11:6037–6044.

19. Oliveira, R. G., E. Schneck, …, M. Tanaka. 2009. Physical mechanisms of bacterial survival revealed by combined grazing-incidence X-ray scattering and Monte Carlo simulation. *C. R. Chim.* 12:209–217.

20. Oliveira, R. G., E. Schneck, …, M. Tanaka. 2010. Crucial roles of charged saccharide moieties in survival of gram negative bacteria against protamine revealed by combination of grazing incidence x-ray structural characterizations and Monte Carlo simulations. *Phys. Rev. E Stat. Nonlin. Soft Matter Phys.* 81:041901.

21. Jeworrek, C., F. Evers, …, R. Winter. 2011. Effects of specific versus nonspecific ionic interactions on the structure and lateral organization of lipopolysaccharides. *Biophys. J.* 100:2169–2177.

22. Clifton, L. A., F. Ciesielski, …, J. H. Lakey. 2016. The effect of lipopolysaccharide core oligosaccharide size on the electrostatic binding of antimicrobial proteins to models of the gram negative bacterial outer membrane. *Langmuir.* 32:3485–3494.

23. Abraham, T., S. R. Schooling, …, J. Katsaras. 2008. Monolayer film behavior of lipopolysaccharide from Pseudomonas aeruginosa at the air-water interface. *Biomacromolecules.* 9:2799–2804.

24. Schneck, E., E. Papp-Szabo, …, M. Tanaka. 2009. Calcium ions induce collapse of charged O-side chains of lipopolysaccharides from Pseudomonas aeruginosa. *J. R. Soc. Interface.* 6 (*Suppl 5*):S671–S678.

25. Rodriguez-Loureiro, I., V. M. Latza, …, E. Schneck. 2018. Conformation of single and interacting lipopolysaccharide surfaces bearing O-side chains. *Biophys. J.* 114:1624–1635.

26. Cornut, I., B. Desbat, …, J. Dufourcq. 1996. In situ study by polarization modulated Fourier transform infrared spectroscopy of the structure and orientation of lipids and amphipathic peptides at the air-water interface. *Biophys. J.* 70:305–312.

27. Boncheva, M., and H. Vogel. 1997. Formation of stable polypeptide monolayers at interfaces: controlling molecular conformation and orientation. *Biophys. J.* 73:1056–1072.

28. Roach, P., D. Farrar, and C. C. Perry. 2005. Interpretation of protein adsorption: surface-induced conformational changes. *J. Am. Chem. Soc.* 127:8168–8173.

29. Clifton, L. A., M. W. Skoda, …, S. A. Holt. 2013. Asymmetric phospholipid: lipopolysaccharide bilayers; a Gram-negative bacterial outer membrane mimic. *J. R. Soc. Interface.* 10:20130810.

30. Jansson, P. E., A. A. Lindberg, …, R. Wollin. 1981. Structural studies on the hexose region of the core in lipopolysaccharides from Enterobacteriaceae. *Eur. J. Biochem.* 115:571–577.

31. Knirel, Y. A., A. N. Kondakova, …, A. S. Shashkov. 2011. Lipopolysaccharide core structures and their correlation with genetic groupings of Shigella strains. A novel core variant in Shigella boydii type 16. *Glycobiology.* 21:1362–1372.

32. Müller-Loennies, S., L. Brade, and H. Brade. 2007. Neutralizing and cross-reactive antibodies against enterobacterial lipopolysaccharide. *Int. J. Med. Microbiol.* 297:321–340.

33. Müller-Loennies, S., B. Lindner, and H. Brade. 2002. Structural analysis of deacylated lipopolysaccharide of Escherichia coli strains 2513 (R4 core-type) and F653 (R3 core-type). *Eur. J. Biochem.* 269:5982–5991.

34. Stenutz, R., A. Weintraub, and G. Widmalm. 2006. The structures of Escherichia coli O-polysaccharide antigens. *FEMS Microbiol. Rev.* 30:382–403.

35. Schneck, E., Y. Gerelli, and S. Micciulla. 2017. Structural investigation of soft interfaces under controlled interaction conditions: development of sample environment and methodology. Institut Laue-Langevin, https://doi.ill.fr/10.5291/ILL-DATA.LTP-9-7.

36. Campbell, R. A., H. P. Wacklin, …, G. Fragneto. 2011. FIGARO: the new horizontal neutron reflectometer at the ILL. *Eur. Phys. J. Plus.* 126:1–22.

37. Schneck, E., I. Berts, …, G. Fragneto. 2015. Neutron reflectometry from poly (ethylene-glycol) brushes binding anti-PEG antibodies: evidence of ternary adsorption. *Biomaterials.* 46:95–104.

38. Kuhl, T. L., J. Majewski, …, G. S. Smith. 1998. A neutron reflectivity study of polymer-modified phospholipid monolayers at the solid-solution interface: polyethylene glycol-lipids on silane-modified substrates. *Biophys. J.* 75:2352–2362.

39. Clifton, L. A., M. W. Skoda, …, J. H. Lakey. 2015. Effect of divalent cation removal on the structure of gram-negative bacterial outer membrane models. *Langmuir.* 31:404–412.

40. Rodriguez-Loureiro, I., E. Scoppola, …, E. Schneck. 2017. Neutron reflectometry yields distance-dependent structures of nanometric polymer brushes interacting across water. *Soft Matter.* 13:5767–5777.

41. Parratt, L. 1954. Surface studies of solids. *Phys. Rev.* 95:359–369.

42. Robertson, W. G., and R. W. Marshall. 1979. Calcium measurements in serum and plasma–total and ionized. *CRC Crit. Rev. Clin. Lab. Sci.* 11:271–304.

43. Raviv, U. 2018. Interacting bacteria surfaces. *Biophys. J.* 114:1515–1517.

44. Phillips, M. C., D. E. Graham, and H. Hauser. 1975. Lateral compressibility and penetration into phospholipid monolayers and bilayer membranes. *Nature.* 254:154–156.

45. Heinrichs, D. E., J. A. Yethon, and C. Whitfield. 1998. Molecular basis for structural diversity in the core regions of the lipopolysaccharides of Escherichia coli and Salmonella enterica. *Mol. Microbiol.* 30:221–232.

46. Sadovskaya, I., J. R. Brisson, …, E. Altman. 2000. Structural characterization of the outer core and the O-chain linkage region of lipopolysaccharide from Pseudomonas aeruginosa serotype O5. *Eur. J. Biochem.* 267:1640–1650.

47. Abraham, T., S. R. Schooling, …, J. Katsaras. 2007. Neutron diffraction study of Pseudomonas aeruginosa lipopolysaccharide bilayers. *J. Phys. Chem. B.* 111:2477–2483.

48. Cousin, F., and A. Menelle. 2015. Neutron reflectivity. *EPJ Web Conf.* 104:1–22.

49. Braslau, A., P. S. Pershan, …, J. Als-Nielsen. 1988. Capillary waves on the surface of simple liquids measured by x-ray reflectivity. *Phys. Rev. A Gen. Phys.* 38:2457–2470.

50. Latza, V. M., I. Rodriguez-Loureiro, …, E. Schneck. 2017. Neutron reflectometry elucidates protein adsorption from human blood serum onto PEG brushes. *Langmuir.* 33:12708–12718.

51. Milner, S., T. Witten, and M. Cates. 1988. Theory of the grafted polymer brush. *Macromolecules.* 21:2610–2619.

52. Jones, R. A. L., and R. W. Richards. 1999. Polymers at Surfaces and Interfaces. Cambridge University Press, Cambridge, UK.

53. Miller, R., V. B. Fainerman, and H. Möhwald. 2002. Comparison of two methods to estimate the standard free energy of adsorption. *J. Surfactants Deterg.* 5:281–286.

54. Campanelli, J. R., and X. Wang. 1999. Dynamic interfacial tension of surfactant mixtures at liquid-liquid interfaces. *J. Colloid Interface Sci.* 213:340–351.

55. Piasecki, D. A., and M. J. Wirth. 1993. Reorientation of acridine orange in a sodium dodecyl sulfate monolayer at the water-hexadecane interface. *J. Phys. Chem.* 97:7700–7705.

56. Chandler, D. 2005. Interfaces and the driving force of hydrophobic assembly. *Nature.* 437:640–647.

Biophysical Journal, Volume *116*

Supplemental Information

Structure and Conformation of Wild-Type Bacterial Lipopolysaccharide Layers at Air-Water Interfaces

Samantha Micciulla, Yuri Gerelli, and Emanuel Schneck

Supporting Information for "Structure and conformation of wild-type bacterial lipopolysaccharide monolayers at air/water interfaces"

S. Micciulla, Y. Gerelli, E. Schneck

Wild-type LPS monolayer stability on Ca^{2+}-free subphase

Figure S1a shows the pressure versus area isotherms for subsequent compression/expansion cycles of a wild-type LPS monolayer spread onto Ca^{2+}-*free* subphase. Similar to the behavior of this monolayer onto Ca^{2+}-*loaded* subphase reported in the manuscript, there is a clear evidence of hysteresis at each cycle, with a relative reduction of the specific area at the highest pressure ($\pi = 45$ mN/M) per cycle between $\approx 3\%$ and $\approx 8\%$.

As for Ca^{2+}-*loaded* LPS, the kinetics of the area reduction shows a dependence on the applied lateral pressure (Figure S1b and c): at an initial pressure of $\pi = 15$ mN/m and constant surface area, the pressure decreases with $d\Pi/dt \approx 0.04$ mN/(m min), while for initial $\pi = 30$ mN/m, the pressure decreases about four times as fast ($d\Pi/dt \approx 0.16$ mN/(m min)).

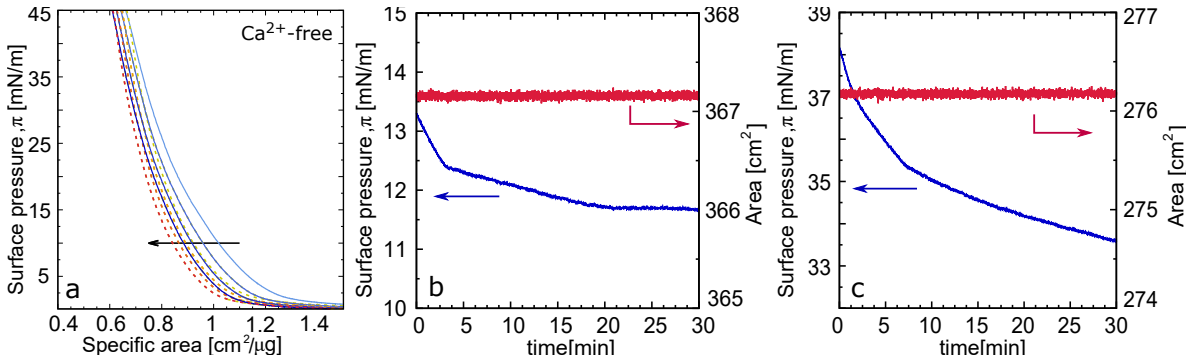

Figure S1: (a): Repeating compression cycles of wild-type LPS monolayers on Ca^{2+}-*free* subphase. (b, c): Evolution of surface pressure over time at constant area starting with an initial surface pressure of about 15 mN/m (b) and about 30 mN/m (c).

Table S1: Best-fit parameters obtained from the analysis of the reflectivity data. The roughness σ for the HC refers to the air/HC interface, while the value for IOS refers to the IOS/water interface. The symbols *n,x* indicate the different contrasts (neutron and X-ray); the symbols *f,l* represent the *free* and *loaded* subphase, respectively.

Parameter	HC	IOS	OSC
$\rho_{i,f}^{n,D_2O}$ [Å^{-2}]	0.4 x 10^{-6}	2.60 x 10^{-6}	2.16 x 10^{-6}
$\rho_{i,l}^{n,D_2O}$ [Å^{-2}]	0.4 x 10^{-6}	2.56 x 10^{-6}	2.12 x 10^{-6}
$\rho_{i,f}^{n,ACMW}$ [Å^{-2}]	0.4 x 10^{-6}	-0.041 x 10^{-6}	-0.034 x 10^{-6}
$\rho_{i,l}^{n,ACMW}$ [Å^{-2}]	0.4 x 10^{-6}	-0.139 x 10^{-6}	-0.011 x 10^{-6}
ρ_i^x [Å^{-2}]	8.0x 10^{-6}	15.2 x 10^{-6}	14.2 x 10^{-6}
d_f [Å]	20 (1)	20 (1)	-
d_l [Å]	15 (1)	17 (2)	-
λ_f [Å]	-	-	119 (10)
λ_l [Å]	-	-	130 (10)
n_f	-	-	1.4 (0.1)
n_l	-	-	1.3 (0.1)
σ_f [Å]	3 (1)	7 (2)	-
σ_l [Å]	3 (1)	14 (2)	-